

Revising the merger scenario of the galaxy cluster Abell 1644: a new gas poor structure discovered by weak gravitational lensing

R. Monteiro-Oliveira,^{1*} L. Doubrawa,^{1,2} R. E. G. Machado,² G. B. Lima Neto,¹
M. Castejon¹ and E. S. Cypriano¹

¹Universidade de São Paulo, Inst. de Astronomia, Geofísica e Ciências Atmosféricas, Depto. de Astronomia, R. do Matão 1226, 05508-090 São Paulo, Brazil

²Universidade Tecnológica Federal do Paraná, Rua Sete de Setembro 3165, 80230-901 Curitiba, Brazil

Accepted XXX, Received YYY in original form ZZZ

ABSTRACT

The galaxy cluster Abell 1644 ($\bar{z} = 0.047$) is known for its remarkable spiral-like X-ray emission. It was previously identified as a bimodal system, comprising the subclusters, A1644S and A1644N, each one centred on a giant elliptical galaxy. In this work, we present a comprehensive study of this system, including new weak lensing and dynamical data and analysis plus a tailor-made hydrodynamical simulation. The lensing and galaxy density maps showed a structure in the North that could not be seen on the X-ray images. We, therefore, rename the previously known northern halo as A1644N1 and the new one as A1644N2. Our lensing data suggest that those have fairly similar masses: $M_{200}^{N1} = 0.90^{+0.45}_{-0.85} \times 10^{14}$ and $M_{200}^{N2} = 0.76^{+0.37}_{-0.75} \times 10^{14} M_{\odot}$, whereas the southern structure is the main one: $M_{200}^S = 1.90^{+0.89}_{-1.28} \times 10^{14} M_{\odot}$. Based on the simulations, fed by the observational data, we propose a scenario where the remarkable X-ray characteristics in the system are the result of a collision between A1644S and A1644N2 that happened ~ 1.6 Gyr ago. Currently, those systems should be heading to a new encounter, after reaching their maximum separation.

Key words: gravitational lensing: weak – dark matter – clusters: individual: Abell 1644 – large-scale structure of Universe

1 INTRODUCTION

The formation of galaxy clusters through the merger of smaller structures is one of the most energetic events known in the Universe, involving an amount of energy of about 10^{64} erg (Sarazin 2004). However, since this process runs over a long period of time (1 – 4 Gyr; e.g. Machado et al. 2015), it does not constitute a cataclysmic event. Nevertheless, merging clusters are a fundamental cornerstone of large-scale structure formation as predicted by our standard cosmological scenario (e.g., Lacey & Cole 1993; Springel et al. 2005) and have an ubiquitous signature, the presence of substructure on clusters of galaxies (e.g., Beers et al. 1982; Jones & Forman 1999; Andrade-Santos et al. 2012).

In spite of the merger process among galaxy clusters being spread over a long period of time, the moments immediately after the pericentric passage are particularly interesting. It has been seen that each cluster component – dark matter, intracluster gas and galaxies – behaves in particular ways during the collision, and a spatial detachment between them can be observed just after the pericentric passage (Markevitch et al. 2004). It has been claimed that a detachment between galaxies and dark matter would be an

observational signature of self-interaction of the dark matter and can provide an astrophysical tool for computing its cross section (σ/m ; e.g. Harvey et al. 2014, 2015). Whether or not such a detachment have been actually detected on data is a matter of debate (Monteiro-Oliveira et al. 2017a; Wittman et al. 2018b).

Even when the merger does not belong to the dissociative class (Dawson 2013), interesting observational features can arise from cluster interactions. For instance, the gravitational perturbation due to an off-axis encounter with a smaller structure may stir the cool gas from the cluster core. This mechanism is known as gas sloshing (Markevitch et al. 2001; Markevitch & Vikhlinin 2007) and may give rise to a spiral of low-entropy cool gas that stems from the cluster core reaching out to as much as a few hundred kpc. Such spirals, which are detectable as an excess in X-ray emission, are not so rare. Based on deep *Chandra* observations, Laganá et al. (2010) showed that this phenomenon may indeed be quite common in the nearby universe. One prominent example of this kind of object is Abell 2052 (Blanton et al. 2011), which has also been modelled by hydrodynamical *N*-body simulations as an off-axis collision (Machado & Lima Neto 2015). In the Perseus cluster, detailed features of the sloshing cold front have also been studied with dedicated simulations (Walker et al. 2018). More recently, a novel technique has allowed measurements of bulk flows of the

* E-mail: rogerionline@gmail.com

Table 1. A1644 mass according to several methods. RVD stands for radial velocity dispersion; WGL for weak gravitational lensing.

Region	M_{200} ($10^{14} h_{70}^{-1} M_{\odot}$)	Method	Reference
Overall	6.0	RVD plus T_X	Ettori et al. (1997)
Overall	$4.50_{+0.80}^{-0.75}$	RVD	Girardi et al. (1998)
Overall	6.9 ± 1.0	Caustic [†]	Tustin et al. (2001)
Overall	$10.40_{+1.01}^{-0.94}$	RVD – NFW	Lopes et al. (2018)
Overall [◊]	$3.99_{-1.59}^{+1.39}$	WGL – NFW	This work (Sec. 3)
A1644N1	3.8 ± 0.6	$M_{500} \times T_X$	Johnson et al. (2010)
A1644N1	$0.90_{-0.85}^{+0.45}$	WGL – NFW	This work (Sec. 3)
A1644S	4.6 ± 0.6	$M_{500} \times T_X$	Johnson et al. (2010)
A1644S	$1.90_{-1.28}^{+0.89}$	WGL – NFW	This work (Sec. 3)
A1644N2*	$0.76_{-0.75}^{+0.37}$	WGL – NFW	This work (Sec. 3)

[†] Inside a radius $R = 2.4$ Mpc

[◊] This value corresponds to the sum of all mass clumps identified by us as A1644 members.

* New structure found in this work.

intracluster medium (ICM), offering direct evidence of gas sloshing in the potential wells of Coma and Perseus (Sanders et al. 2020).

In this work, we will devote our attention to the nearby galaxy cluster Abell 1644 (hereafter A1644; $\bar{z} = 0.047$, Tustin et al. 2001), which we show in Fig. 1. An *Einstein* X-ray image by Jones & Forman (1999) showed A1644 as a bimodal structure. Johnson et al. (2010) named the components after their positions as A1644S, the main (southern) structure, and A1644N on the North side. Both have their X-ray peaks spatially coincident with a giant elliptical galaxy or their respective brightest cluster galaxies (BCGs). Reiprich et al. (2004a), using XMM-Newton data, argued that we are seeing the system after an off-axis collision of those substructures. In Table 1 we present a compilation of estimated masses for A1644 available in the literature.

Regarding the optical components, the substructures of A1644 are somewhat less clearly visible. Whereas Dressler & Shectman (1988) found evidence for substructure in A1644 based on the analysis of 92 redshifts, Girardi et al. (1997) classified A1644 as a single system, based on an analysis combining both galaxy positions and redshifts. A similar conclusion was proposed by Tustin et al. (2001) who measured redshifts for 144 cluster members. They found a rather larger than expected radial velocity dispersion, $\sigma \sim 1000$ km s⁻¹, which suggested a system out of the equilibrium state (e.g. Monteiro-Oliveira et al. 2018; Pandge et al. 2019). However, the authors found no evidence for the presence of substructure in this cluster, in contrast with the scenario suggested by X-ray observations.

High spatial resolution observations with the *Chandra* satellite analysed by Johnson et al. (2010) provided straightforward arguments in favour of the post-collision state of A1644. Notably, the authors detected the presence of a cold front (Markevitch & Vikhlinin 2007) at the edge of the Southern subcluster with a spiral morphology. They proposed a merger scenario where an off-axis passage of A1644N by A1644S was responsible for pushing the gas of the latter out the bottom of its gravitational potential well. This gas was driven into an oscillating motion (sloshing) which

Table 2. Characteristics of our imaging data observed at Dark Energy Camera. The deepest r' band was chosen as the basis for our weak lensing analysis.

Band	Total exposure (h)	Mean air mass	Seeing (arcsec)
g'	0.5	1.20	1.21
r'	1.0	1.07	1.09
i'	0.4	1.12	1.08

generated the observed spiral-like structure. Based on a comparison with generic hydrodynamical simulations (Ascasibar & Markevitch 2006), they estimated that the pericentric passage between A1644S and A1644N happened about 700 Myr ago.

In spite of the wealth of analysis already devoted to A1644, a mapping of the total mass distribution is still lacking in the literature. One plausible reason is that weak lensing studies of such low-redshift systems are challenging due to the intrinsic low signal (e.g. Cypriano et al. 2001, 2004). Nevertheless, we have successfully recovered the mass distribution of a galaxy cluster at a similar redshift (Abell 3376; Monteiro-Oliveira et al. 2017b).

This paper presents the first weak lensing study fully dedicated to A1644. From deep and large field-of-view multiband images (g' , r' , and i'), we recovered the mass distribution of the cluster. Complementarily, the redshift catalogue available in the literature allowed us to revisit the cluster dynamics in order to solve the inconsistency between the distinct cluster morphologies proposed previously by either X-ray or radial velocity observations. From these combined analyses (weak gravitational lensing plus cluster dynamics), we were able to characterize dynamically each component of the system, including substructures that were not identified in previous studies. To go beyond our present understanding of this cluster's dynamical history, we have performed a tailor-made hydrodynamical simulation in order to describe the timeline of the collision. This tool is fundamental to link the observational findings of this paper and the remarkable X-ray features seen in A1644 to the process of large-scale structure formation.

This paper is organized in the following way. In Section 2 we perform the photometric analysis. The reconstruction of the mass field through the weak gravitational lensing is introduced in Section 3. The dynamical view, based on the redshift catalogue is presented next, in Section 4. The set-up as well as the results of our hydrodynamical simulation showing the best model for the collisions that occurred in A1644 are in Section 5. Finally, our main findings are discussed in Section 6 and summarised in Section 7.

Throughout this paper we adopt the standard Λ CDM cosmology, represented by $\Omega_m = 0.27$, $\Omega_{\Lambda} = 0.73$, $\Omega_k = 0$ and $h = 0.7$. At the mean cluster redshift of $z = 0.047$, we then have a plate scale of 1 arcsec equal 0.926 kpc and an angular diameter distance of 191.1 Mpc (Wright 2006).

2 PHOTOMETRIC ANALYSIS

2.1 Imaging data

The present imaging data were obtained on February 1, 2014 with the Dark Energy Camera (DECam) mounted at the Victor Blanco 4m-telescope (Proposal ID: 2013B-0627 within the SOAR Telescope time exchange program; PI: Gastão Lima Neto). The observational details are shown in Table 2.

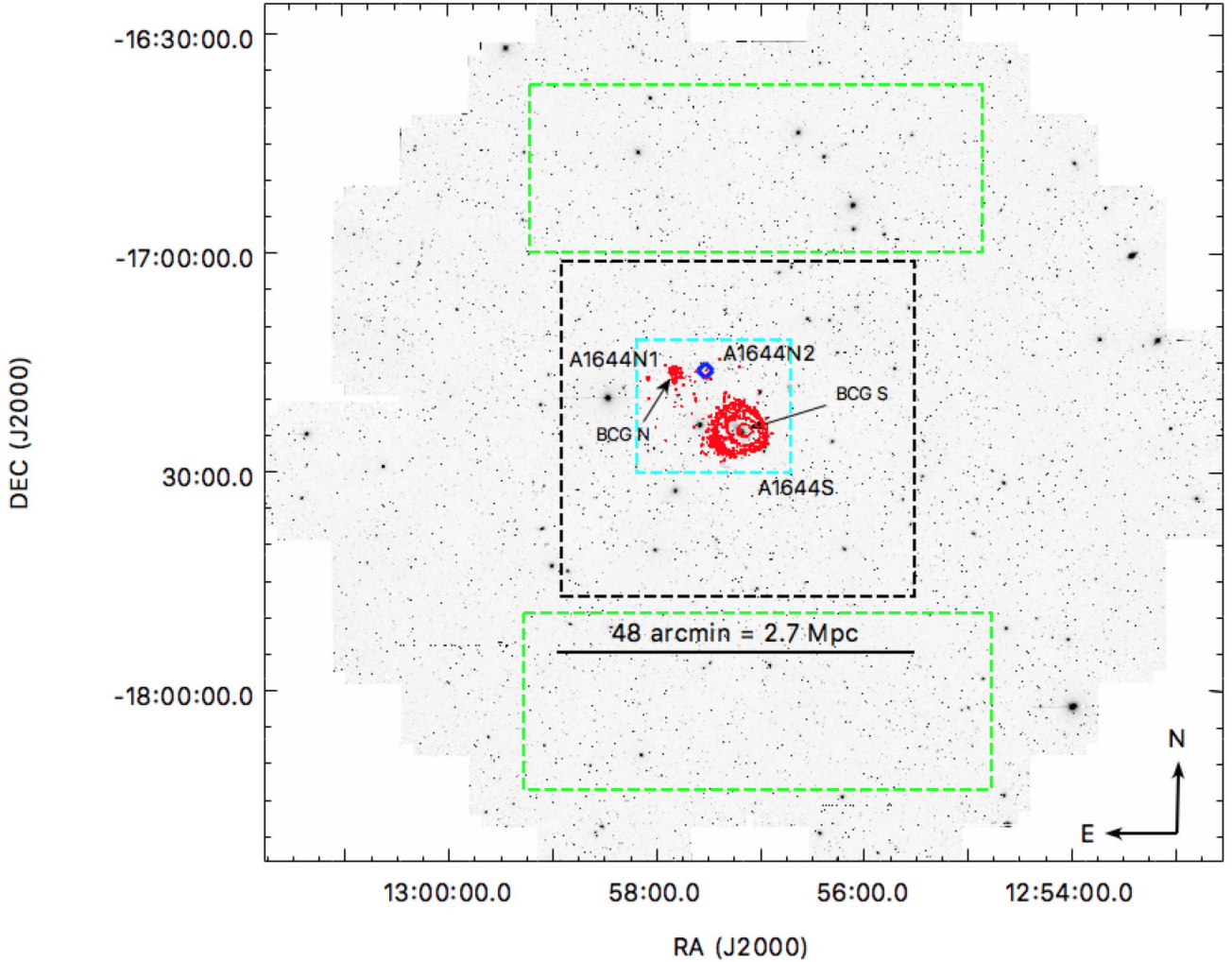


Figure 1. Optical image of the A1644 field in the r' band, taken with the Dark Energy Camera at Victor Blanco telescope. The red contours correspond the *Chandra* X-ray image. The X-ray emission is bimodal and each peak coincides with the position of a giant elliptical galaxy (BCG S and BCG N), located at the centre of the main (A1644S) and northern (A1644N1) structures. The new substructure found by weak lensing (Sec. 3) is labelled as A1644N2 (blue diamond). Green and cyan dashed boxes delimit the regions used the identification of the cluster red sequence galaxies (Sec. 2). The black dashed line box encloses the region of interest (48 arcmin^2), which we will analyse throughout the paper.

We used standard procedures (Valdes et al. 2014) for image reduction/combination and astrometric calibration. The latter resulted in a positional rms for Adelman-McCarthy (2011) catalogue stars of $0.6 \pm 0.5 \text{ arcsec}$, which is more than enough for the purposes of the current analysis.

Observations were made under non-photometric conditions. This is acceptable as accurate absolute photometric calibration is not a strong requirement for lensing, which is more concerned with galaxy shapes and positions. In order to get an approximate calibration we used average values of the airmass extinction coefficients provided by the observatory staff (Walker, private communication), which resulted in the following zero point magnitudes: $g_0 = 31.31 \pm 0.05$, $r_0 = 31.53 \pm 0.05$ and $i_0 = 31.73 \pm 0.04$.

We used SExtractor in double image mode to create object catalogues. Detections were made in the deeper r' image. Galaxies were then selected with two criteria: (i.) $r' \leq 19.0 \text{ CLASS_STAR}$

index lower than 0.8 and (ii.) $r' > 19.0$ with their full width at half-maximum (FWHM) greater than 1.3 arcsec, a value 0.2 arcsec above the seeing to ensure the selection of well-resolved objects.

2.2 Identification of the red sequence cluster galaxies

Galaxies correspond only to $\sim 5\%$ of the total cluster mass but their correlation in the projected space is one of the few ways to trace a cluster in the optical band. Another useful tracer of the red cluster members is their well-known correlation in the colour-colour map (e.g. Medezinski et al. 2010, 2018). We identified the A1644 red-sequence locus on an $(r' - i') \times (g' - r')$ diagram by applying a statistical subtraction method (more details in Monteiro-Oliveira et al. 2017b).

We used the galaxies within the green boxes in Fig. 1 as a representation of the field population and the ones inside the cyan

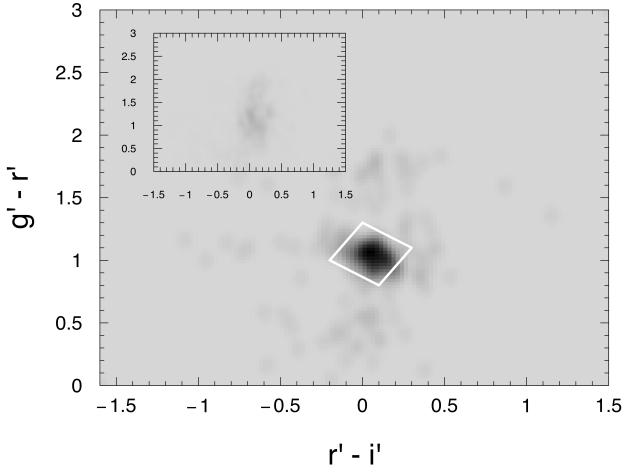


Figure 2. Colour-colour diagram of the galaxies located at the innermost region of the cluster field (cyan box of Fig. 1). Due to the fact that they present homogeneous photometric properties, the red cluster member galaxies form a density peak in this space, thus defining the cluster member *locus*. In this plot, galaxies are brighter than $r' = 19.5$, considering the magnitude limit for selection of cluster members. The inset panel presents the same plot with the same linear grey-scale, but for the galaxies in the control areas (green boxes in Fig. 1).

box as field plus cluster populations. This central region presents a galaxy density excess in relation to the control (field) ones up to magnitude $r' = 19.5$, which we then took as a faint limit for A1644 red-sequence galaxies. In Fig. 2 we show this density excess in the colour-colour space. The region with the highest excess corresponds to the locus of the A1644 early-type galaxies.

There is a total of 613 galaxies on this colour-colour locus over the entire optical image. We call those ‘photometric members’, yet knowing that this sample is not free of contamination and that it does not include blue members. Their r' projected galaxy luminosity distribution is presented in Fig. 3. This ‘luminosity map’ is a 30 arcsec pixel-based image done by smoothing each galaxy by a bidimensional, circular Plummer profile (or an index 5 polytrope) kernel with a core radius of 1 arcmin, following O’Mill et al. (2015) and Machado & Lima Neto (2015).

Although we will perform a more quantitative analysis of the red cluster galaxy luminosity peaks after the lensing analysis in Sec. 3.2, there are obvious features in Fig. 3 that should be pointed out. There X-ray maxima (A1644S and A1644N1) have their luminosity counterparts. There is one very prominent peak in the red member luminosity map with no X-ray counterpart. We label this substructure as A1644N2.

3 WEAK LENSING ANALYSIS

We used weak lensing techniques to recover the projected mass distribution on the A1644 field as estimate masses of its substructures, following the procedures we used in the study of other merging clusters Monteiro-Oliveira et al. (2017a,b, 2018). Below we describe the data characteristics, treatment, and modelling. For a review of the fundamentals of lensing, we refer the reader to excellent reviews that can be found in the literature, such as Mellier (1999), Schneider (2005), and Meylan et al. (2006).

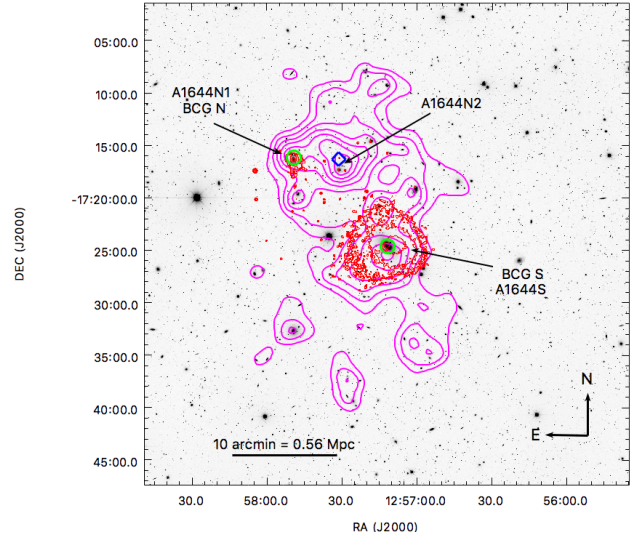


Figure 3. Optical image overlaid with contours of the cluster member luminosity map (magenta) and of the X-ray emission (red). Both BCG S and BCG N (green circles) lie in local peaks of the luminosity map. Furthermore, this shows a third relevant concentration west of A1644N1, within the *Chandra* field but with no visible X-ray emission. We named this substructure as A1644N2. As we show in the text (Sec. 3.2), this galaxy concentration coincides with the position of a dark matter clump (blue diamond). In addition, we found other less significant clumps surrounding the central region. This image is of the black box area defined in Fig. 1.

3.1 Source selection and shape measurement

The background or source galaxies images constitute the raw material for weak lensing studies because those respond to the gravitational lensing effect caused by the galaxy cluster mass. This effect manifests as a slight shape distortion on the images of the aforementioned galaxies. Therefore, a careful selection of source galaxies is crucial for a successful weak lensing analysis.

A1644 is located at a very low redshift ($\bar{z} = 0.047$, see Sec. 4), therefore we expect most galaxies in our image to be in the cluster background. In fact, for a galaxy cluster at a similar distance, we found that foreground galaxies correspond to less than 0.2% of the CFHTLS¹ catalogue (Monteiro-Oliveira et al. 2017b). This prompted us to consider as source all galaxies fainter than $r' = 21$ and not in the red cluster locus on the colour-colour space (Fig. 2). Remembering that we could not detect an excess associated with clusters galaxies fainter than $r' = 19$, we should have a very complete and uncontaminated source sample.

To estimate the average surface critical density, that depends on both the cluster and source redshifts, we applied the same cuts on the CFHTLS catalogue, with photometric redshifts, and found $\Sigma_{cr} = 9.6 \times 10^9 M_{\odot} \text{ kpc}^{-2}$.

The next step is to map the point spread function (PSF), which affects all image shapes across the r' band image used for shape measurements. To do that, we identified bright unsaturated stars spread across the field, split them into nine frames and modelled their shapes with the Bayesian code IM2SHAPE (Bridle et al. 1998). Besides modelling individual objects as a sum of Gaussians with

¹ Canada-France-Hawaii Telescope Legacy Survey; <http://www.cfht.hawaii.edu/Science/CFHTLS/>

an elliptical basis, this code also deconvolves the effects of the local PSF.

For the PSF mapping, the star profiles are modelled as single Gaussians and no PSF deconvolution is done. The main results of this process are the ellipticity components e_1 , e_2 , and a size parameter, related to the seeing. Then, the discrete sample of parameters was spatially interpolated across the field with the thin plate spline regression (Nychka et al. 2014) built-in R environment (R Core Team 2014) to create a continuous function. Stellar data with discrepant values were removed in 3 iterative steps; at each step, objects with the 10 per cent largest absolute residuals were discarded. The measured stellar ellipticities and respective residuals after the spatial interpolation are presented in Fig. 4.

The averaged ellipticity of all field was $\langle e_1 \rangle = 0.014$ with $\sigma_{e_1} = 0.010$ and $\langle e_2 \rangle = 0.001$ with $\sigma_{e_2} = 0.010$. As stars are points sources for all practical aspects all deviations from null values are due to the PSF effect. As illustrated by Fig. 4, our model performed a good match with the data as shown by the very small averaged residual (10^{-5}) and standard deviation (0.003).

Given the PSF field at each point of the image, we used `IM2SHAPE` over galaxies, modelling them as two Gaussians with the same elliptical base. Now the software produces PSF-free ellipticities and respective uncertainties. The latter are used as a quality criterion. Objects with $\sigma_e > 2$ or those having evidence of blending were removed from the source sample.

3.2 The projected mass distribution

3.2.1 The signal-to-noise shear map

The ellipticities of the galaxies can be seen as noisy probes of the shear field, as each galaxy has its own non-lensing related ellipticity. The shear field can then, through techniques, be turned into a convergence field or a mass map. Here we created a signal-to-noise ratio (S/N) map of structures by averaging the tangential ellipticity e_+ in relation of a grid of points, for the N_{θ_0} galaxies inside a radius θ_0 , as prescribed by the mass aperture statistic (Schneider 1996),

$$S/N = \frac{\sqrt{2}}{\sigma_e^2} \frac{\sum_{i=1}^{N_{\theta_0}} e_{+i}(\theta_i) \mathcal{Q}_{\text{NFW}}(\theta_i, \theta_0)}{\left[\sum_{i=1}^{N_{\theta_0}} \mathcal{Q}_{\text{NFW}}^2(\theta_i, \theta_0) \right]^{1/2}}, \quad (1)$$

where θ_i is the position of the i^{th} source galaxy and σ_e is the quadratic sum of the measured error and the intrinsic ellipticity uncertainty, estimated as 0.35 for our data. We adopted the NFW filter (Schirmer 2004),

$$\mathcal{Q}_{\text{NFW}}(\theta_i, \theta_0) = [1 + e^{a-b\chi(\theta_i, \theta_0)} + e^{-c+d\chi(\theta_i, \theta_0)}]^{-1} \times \frac{\tanh[\chi(\theta_i, \theta_0)/\chi_c]}{\pi\theta_0^2[\chi(\theta_i, \theta_0)/\chi_c]}, \quad (2)$$

with $\chi = \theta_i/\theta_0$, which describes approximately an NFW shear profile. Hettterscheidt et al. (2005) suggest, as optimized parameters for halo detection, $a = 6$, $b = 150$, $c = 47$, $d = 50$, and $\chi_c = 0.15$, which we adopted. We also considered the radius $\theta_0 = 8$ arcmin. The resulting S/N map can be seen in Fig. 5.

In a case like A1644, which is not a very massive cluster and is situated at a low redshift, that does not favour the lensing signal, its structures do not stand out in the shear S/N map. In such a case several smaller mass background structures plus line-of-sight superpositions (Yang et al. 2013; Liu & Haiman 2016) can create similar S/N features in the map and thus the noisy appearance we see in Fig. 5. None the less the map shows a clear high S/N clump

Table 3. Relevant quantities for the weak lensing convergence map reconstruction.

N_g (gal. arcmin $^{-2}$)	10.7
ICF FWHM (arcmin)	2.8
σ_κ^*	0.011

* Noise level in the convergence map.

spatially coincident with the BCG S. Also, BCG N is superposed with an arched clump that stretches mainly in the east-west direction. Besides, there is some amount of significance halfway between the two BCGs, whose pertinence to the targeted galaxy cluster will be better investigated.

3.2.2 Convergence map

To create a convergence (κ) or projected mass map of the field we resorted to the maximum entropy algorithm (Seitz et al. 1998) of the Bayesian code `LENSENT2` (Marshall et al. 2002). It works by maximizing the evidence of the reconstructed mass field in relation to the data. In order to take into account the noisiness of individual measurements and prevent overfitting, `LENSENT2` uses a Gaussian intrinsic correlation function (ICF). We have tested reconstructions done with a $\sigma_{\text{ICF}} \in [70 : 210]$ arcsec range.

For each realization of a mass map, given the ICF width, we did an automatic peak search (which is described next) and compared the number of detected clumps above 1σ , 2σ , and 3σ . We found that the number of peaks detected above 3σ remained approximately the same for $\sigma_{\text{ICF}} \geq 170$ arcsec (~ 2.8 arcmin), which we adopted as bona fide. The convergence map is presented in Fig. 6 and the mass reconstruction characteristics are shown in Table 3.2.2.

The S/N and the convergence maps are qualitatively very similar, both showing a wealth of structures. Some common features stand out, however; in particular, the peaks #2 and #6 of the κ map, which are also present in the S/N map, and can be associated with A1644S and A1644N1, respectively, which we already identified in the member luminosity and X-ray maps. The situation is not so clear for the remaining peaks and will be further investigated.

3.2.3 Characterization of the mass peaks

To compute the exact position of each mass clump or peak centre, we applied an automatic procedure. First, the algorithm searched for local maxima in the convergence map within a moving circular window with 2.3 arcmin radius, which allows measuring individual peak statistics (e.g. $\bar{\kappa}$) without any overlapping.

The peak centre position is then defined as the pixel-weighted mean inside the circular region. Its significance ν is the ratio between the local maxima κ_{max} and the noise level σ_κ . To measure the latter, we have performed 100 realizations of the mass distribution removing the cluster lens signal. This was done by rotating each galaxy ellipticity by a random angle $[0, 180]$. This procedure also allowed us to identify spurious peaks caused by noise fluctuations.

The averaged noise level can be seen in Table 3.2.2 and a summary of the detected and expected number of spurious peaks are in Table 4. As we can see, the probability to detect a spurious peak above $4\sigma_\kappa$ is almost zero. In Table 5, we describe the most significant ($\nu > 4$) peaks within the convergence map. Some of those maybe be related to A1644 but most should be typical field features of such maps (Yang et al. 2013; Liu & Haiman 2016).

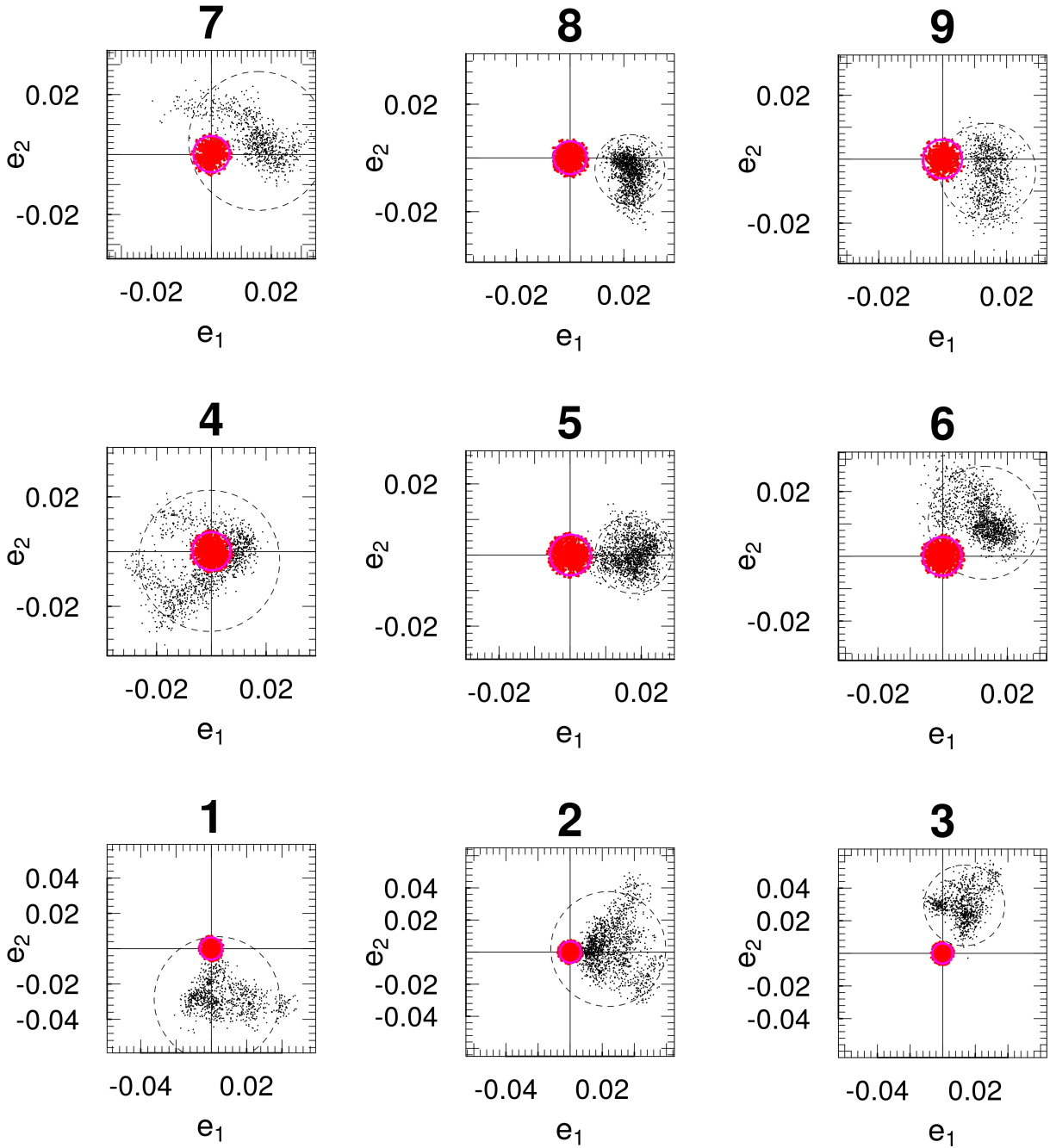


Figure 4. PSF ellipticity. The black dots are the raw components e_1 and e_2 obtained from the stars and the red ones the residuals between those and the PSF ellipticity map for the 9 segments that composes a full DECam image. Dashed circles enclose 95% of the data. The averaged residuals are 10^{-5} for e_1 and e_2 with a standard deviation of 0.003 for both.

3.2.4 Correlation with cluster luminosity map

The most straightforward way to identify which of the peaks in the convergence map belong to A1644 is to identify possible counterparts in the luminosity map. It assumes that mass and (optical) light will follow each other, which tends to hold even for merging clusters (Clowe et al. 2004, 2006).

We search for peaks in the red-sequence map in a similar manner than we did in the κ map, this time with a circular window

of 1.2 arcmin radius. We found 11 clumps (labelled A–K) with significance greater than $3.5\sigma^2$ (σ being the standard deviation of all pixels). We also computed the nearest mass clump and the respective distance. These values are presented in Table 6. In Fig. 6

² This slightly lower threshold was chosen so that we could find viable counterparts for all κ peaks.

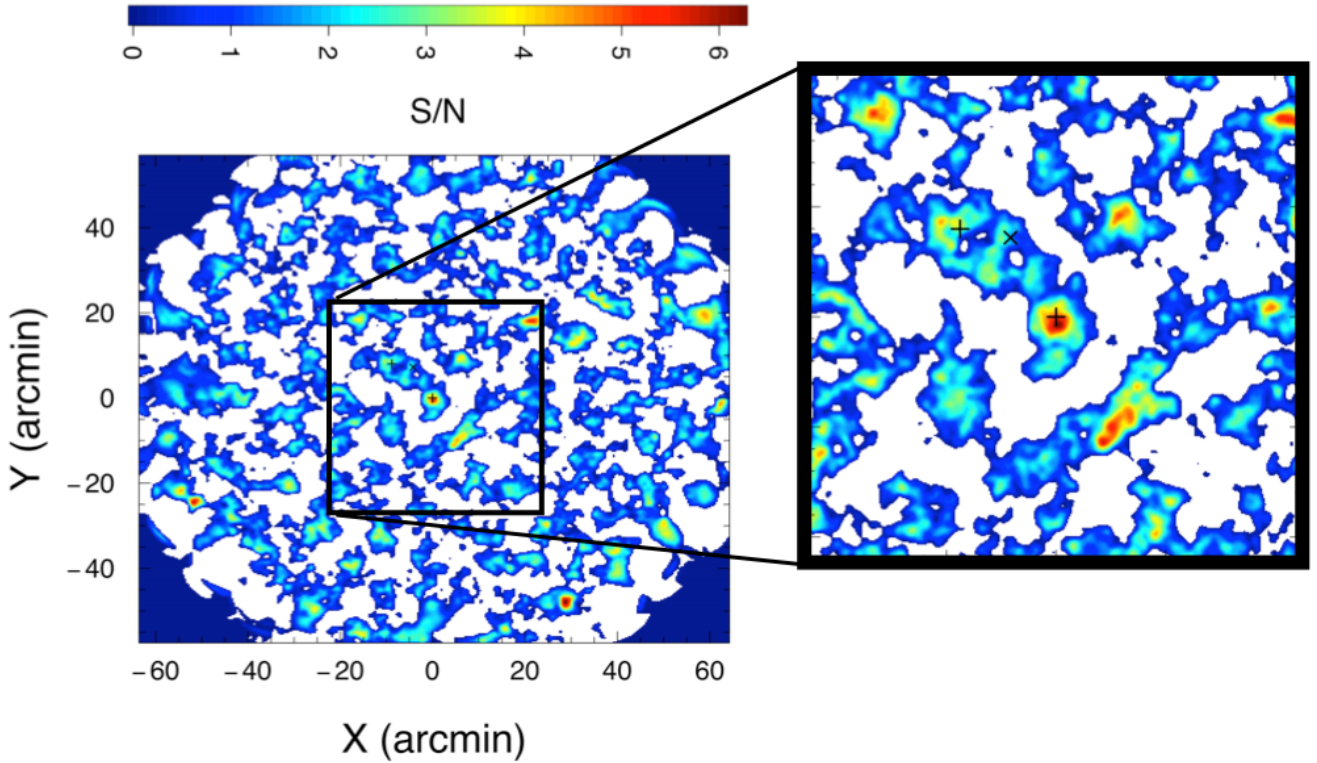


Figure 5. Signal-to-noise map obtained through the mass aperture statistic highlighting A1644 central region (Fig. 1), according to the cluster member luminosity distribution. White regions correspond to negative S/N. The position of the two BCGs and the galaxy clump A1644N2 are marked with “+” and “x”, respectively. The field is densely populated by mass peaks, most of them, however, due to the background large-scale structure.

Table 4. Summary of our search for mass peaks in the convergence map.

Threshold interval (σ_κ)	Number of detected peaks	Expected number of spurious peaks
[2, 3[4	2.2 ± 2.9
[3, 4[5	0.2 ± 0.5
≥ 4	18	0.01 ± 0.10

we show the r' projected galaxy luminosity distribution overlapped with the projected mass map.

From Fig. 6 and Table 6 we can see that A1644S and A1644N1 are, as expected, noticeable. They are associated with the luminosity peaks B (#2) and C (#6), respectively, which offset of only 42 and 49 kpc^3 between luminosity and projected density peaks.

The most prominent peak in the luminosity map (A), is the one we named A1644N2 in Sec. 2.2. It is clearly associated with the mass density peak #9, only 51 kpc (55 arcsec) away. Due to the absence of any detectable X-ray emission from this region on the *Chandra* image (Fig. 3), A1644N2 can be characterized as gas-poor, if not gas-free.

Despite the absence of a dominant red galaxy, as seen in A1644S and A1644N1, there is a large number of galaxies in A1644N2. The significance rank of luminosity presented in Table 6

does not change significantly when we vary the smoothing scale. For smaller scales (5, 10 and 15 arcsec) clump A is subdivided into two others which became the first and second most significant. For larger scales (30 and 40 arcsec), clumps A and C are merged into a single and most significant clump.

On a lower significance level, we can find two other A1644 substructures by associations between peaks in the red members luminosity and mass density maps: G-#10 (offset by 78 kpc) and H-#16 (39 kpc). Both are on the outskirts of the A1644’s core formed by S, N1 and N2 substructures. They are both outside the *Chandra* image field of view.

All other galaxy concentrations are, at least, 145 kpc away from the nearest mass clump, about three times more than A-#9, B-#2 and C-#6, and thus their physical associations cannot be taken for granted. E-#5 is one of such cases. It is within the core of the cluster and is one of the highest peaks of the density mass map. It is also well inside the *Chandra* field of view and has no detectable X-ray emission.

Another case is I-#3. It resembles H-#16 and G-#10 by being outside the cluster core and the X-ray image as well. The projected distance between mass and light centres is indeed larger (146 kpc), but as it is in a much less crowded region of the field, their association seems plausible.

In Section 4 we will use the radial velocity of cluster members in an attempt to solve, among other issues, the question about the pertinence or not of the aforementioned haloes to A1644.

In order to check whether some of the mass map density peaks

³ Projected distances assuming A1644 redshift.

Table 5. Statistics of the identified mass clumps. The first five columns refer to the clump ID [1], the peak centre coordinates [2–3], the peak significance $\nu = \kappa_{\max}/\sigma_{\kappa}$ [4] and the mean convergence inside a circular region [5]. The mass modelled according to our model are presented in column [6] where absent values correspond to those peaks for which our model was not able to produce reliable results (mostly because of the relatively low significance and the location close to field border). Relevant comments on each mass clump are shown in the last column [7].

Clump	α (J2000)	δ (J2000)	ν	$\bar{\kappa}$ (< 2.3 arcmin)	M_{200} ($10^{14} M_{\odot}$)	Comments
1	12:55:42	-17:06:47	13.0	0.081	–	Border/background
2	12:57:12	-17:24:47	10.6	0.071	$1.90^{+0.89}_{-1.28}$	A1644S
3	12:56:51	-17:34:41	9.9	0.065	$3.37^{+1.40}_{-2.06}$	A1644 candidate
4	12:58:19	-17:06:21	8.7	0.053	–	Border/background
5	12:57:37	-17:20:44	8.0	0.054	$0.87^{+0.43}_{-0.82}$	A1644 candidate
6	12:57:54	-17:16:20	7.4	0.055	$0.90^{+0.45}_{-0.85}$	A1644N1
7	12:56:45	-17:15:48	7.2	0.048	$0.81^{+0.40}_{-0.74}$	background
8	12:55:51	-17:24:15	6.4	0.042	–	Border/background
9	12:57:31	-17:16:21	6.2	0.046	$0.76^{+0.37}_{-0.75}$	A1644N2
10	12:57:16	-17:10:51	5.6	0.036	$0.56^{+0.28}_{-0.55}$	A1644 candidate
11	12:58:23	-17:30:13	5.4	0.034	–	Border/background
12	12:55:46	-17:29:14	4.6	0.035	–	Border/background
13	12:58:38	-17:22:48	4.6	0.032	–	Border/background
14	12:56:34	-17:43:40	4.4	0.033	–	Border/background
15	12:57:50	-17:10:20	4.3	0.029	–	background
16	12:58:40	-17:36:10	4.2	0.034	–	A1644 candidate
17	12:57:48	-17:32:42	4.2	0.029	–	Border/background
18	12:57:50	-17:05:52	4.1	0.028	–	Border/background

would be associated with some massive background structure, we looked for associations between them and overdensities in the background galaxy sample. We failed to find any. Our interpretation is, therefore, that most of the κ peaks not associated with A1644 should be due to constellations of ($\lesssim 10^{13} M_{\odot}$) background haloes which dominate the population of low peaks in the field (e.g. [Yang et al. 2013](#); [Liu & Haiman 2016](#); [Wei et al. 2018](#)).

3.3 Mass estimation

3.3.1 Mass field modelling

The weak lensing masses of the individual mass clumps are in general better recovered by fitting physically motivated profiles. In crowded fields, such as the one we are dealing with, it can be done individually as there will be clear covariances between the several substructures. Here we will fit simultaneously 18 structures, which we will treat as dark matter haloes centred on the peaks with $\nu > 4$ found in the κ map.

The weak gravitational lensing effect induced on each source galaxy is a combination of those generated by each of the individual mass clumps. Here, we will adopt a simplified model in which all of them are located at the same cluster redshift. It is easier, in this case, to deal with the Cartesian components of the reduced shear, g_1 and g_2 , which are obtained by projecting the lens generated tangential

component g_+ by the lensing convolution kernel,

$$D_1 = \frac{y^2 - x^2}{x^2 + y^2}, \quad D_2 = \frac{-2xy}{x^2 + y^2}, \quad (3)$$

where x and y are the Cartesian coordinates relative to the lens centre which was considered at the respective mass peak position.

The resulting reduced shear that will affect the image of each source galaxy can be written as

$$g_i = \sum_{k=1}^{N_{\text{clumps}}} g_i^k, \quad (4)$$

with $i \in \{1, 2\}$. As we modelled the mass peaks in the region of interest, $N_{\text{clumps}} = 18$.

The model adopted is as a single circular NFW profile per clump or halo ([Navarro et al. 1996, 1997](#)). The χ^2 -statistic is then

$$\chi^2 = \sum_{j=1}^{N_{\text{sources}}} \sum_{i=1}^2 \frac{[g_i(M_{200}, c) - e_{i,j}]^2}{\sigma_{\text{int}}^2 + \sigma_{\text{obs},j}^2}, \quad (5)$$

where $g_i(M_{200}, c)$ is the reduced shear (Eq. 4) produced by all the NFW haloes over the position of a given source galaxy, M_{200} is the mass within a radius where the mean enclosed density is equal to $200 \times$ the critical density of the Universe, c is the halo concentration parameter, $e_{i,j}$ is the measured ellipticity parameter per galaxy, $\sigma_{\text{obs},j}$ is its measurement uncertainty and σ_{int} is the shape noise, taken as ~ 0.35 for our data.

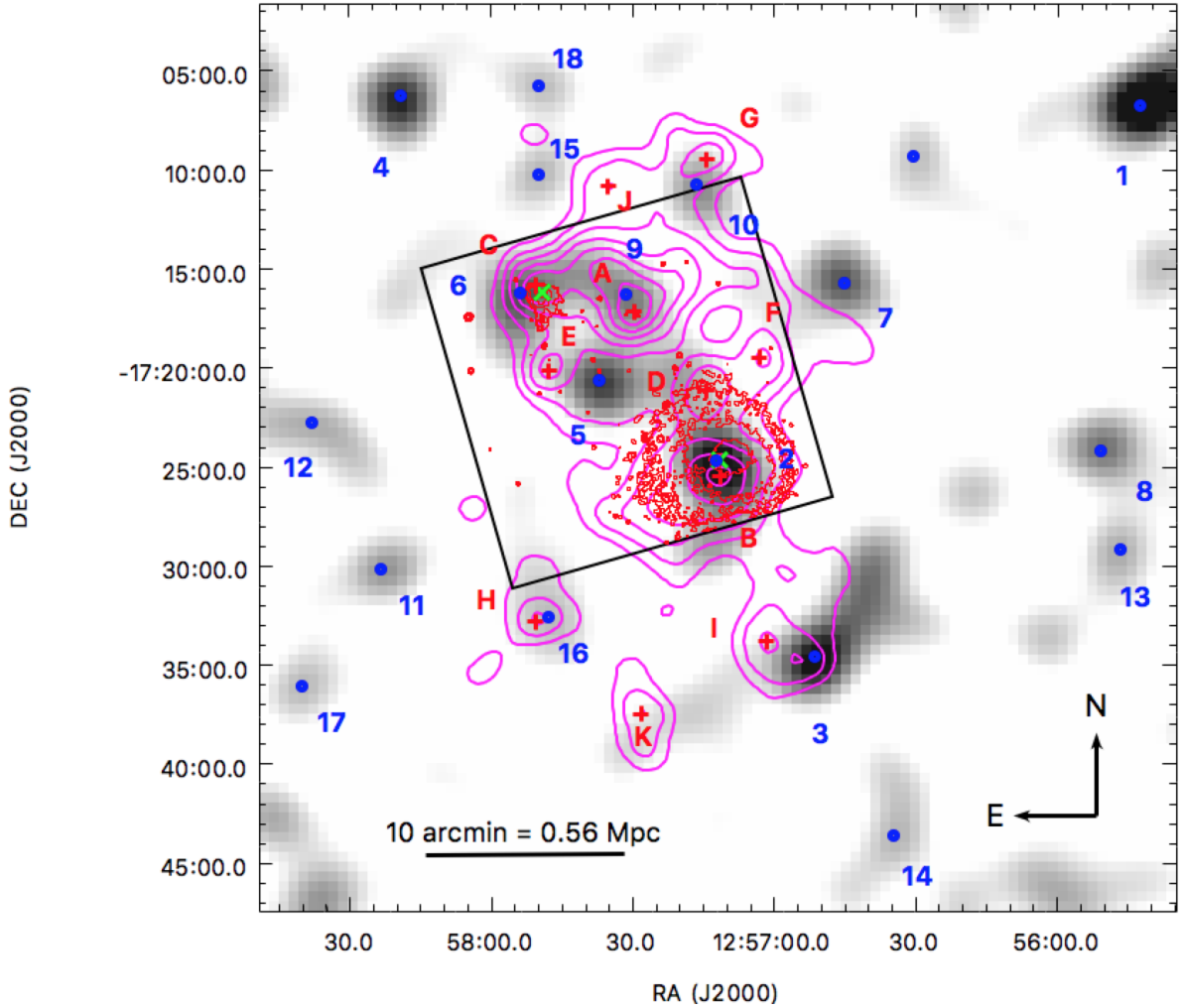


Figure 6. Mass-luminosity correlation. Projected mass map (grey-scale) overlaid with the luminosity density distribution of red cluster members (magenta contours). Blue dots mark the mass peak centres (labelled 1–18) whereas the red “+” are placed at the galaxy clumps centre (A–H). BCGs positions are marked with green “x” symbols. The black box shows the X-ray *Chandra* image field of view.

The likelihood can now be written as

$$\ln \mathcal{L} \propto -\frac{\chi^2}{2}. \quad (6)$$

There are $2 \times N_{\text{clumps}}$ free parameters in our model which can lead to instabilities in the final model. We thus opt to reduce this number in half by adopting the $M_{200} - c$ relation by Duffy et al. (2008):

$$c = 5.71 \left(\frac{M_{200}}{2 \times 10^{12} h^{-1} M_{\odot}} \right)^{-0.084} (1+z)^{-0.47}. \quad (7)$$

Given that the above relation having a scatter, we opt to not include it in our model in order to keep the parameter space to a minimum, given the complexity of the field.

Finally, the posterior can be written as

$$\Pr(M_{200}|\text{data}) \propto \mathcal{L}(\text{data}|M_{200}) \times \mathcal{P}(M_{200}), \quad (8)$$

where we adopted an uniform prior $\mathcal{P}(M_{200})$, $0 < M_{200} \leq 8 \times 10^{15} M_{\odot}$.

3.3.2 Model assessment

Before stating the results, given the complexity of this field, mostly driven by the low signal from the very nearby cluster, we felt the need to further ensure the reliability of the whole modelling procedure. We created a synthetic reduced shear field by positioning NFW lenses at the same position of the eighteen detected mass density peaks plus a population of source galaxies also at the same position as the ones in our background sample.

For this model, we got the mass of A1644S from the X-ray mass by Johnson et al. (2010)⁴. The remaining masses were set by multiplying this value to the ratio of the peak heights (ν/ν_{A1644S} ; Table 5). The reduced shear components for each galaxy were then set as the sum of the contributions of each of the lenses. We did not add anything else to take into account the shape or measurement noises.

⁴ The value was converted from M_{500} to $M_{200} = 4.65 \times 10^{14} M_{\odot}$ (following an NFW profile) to be used here.

Table 6. Characteristics of the peaks found in the luminosity map of red-sequence galaxies. Columns are, respectively: ID, position, significance in units of σ (standard deviation of all pixels), the nearest mass peak ID and the respective projected distance assuming A1644 redshift.

Clump ID	α (J2000)	δ (J2000)	S (σ)	Nearest mass clump	Distance (kpc)
A	12:57:30	-17:17:12	5.8	#9	51
B	12:57:11	-17:25:32	5.0	#2	42
C	12:57:50	-17:15:51	4.9	#6	49
D	12:57:14	-17:21:12	4.4	#2	201
E	12:57:48	-17:20:11	4.2	#5	145
F	12:57:03	-17:19:32	4.1	#7	314
G	12:57:14	-17:09:32	3.8	#10	78
H	12:57:51	-17:32:51	3.6	#16	39
I	12:57:02	-17:33:52	3.6	#3	146
J	12:57:35	-17:10:52	3.5	#15	195
K	12:57:28	-17:37:32	3.5	#16	372

Given the high degree of idealisation idealization of this simulation, one should expect all the results to be very close to the true ones, and it happens for those with higher peak heights and on the core of the cluster.

However, in some cases, the recovered representative mass value⁵ was considerably larger than the reference ($> 35\%$). We mention, as an example, the case of clump #14 whose measured mass was 56% larger than stated in the synthetic catalogue. These mass clumps have in common: (i) their relative low significance ν and/or (ii) their proximity to the border of the region considered for modelling. Based on these arguments, we decided not to consider the MCMC results for the clumps with $\nu < 5.5$, nor those located close to the borders.

3.3.3 Results

We restricted the source galaxies used in the model to those contained in the central region of interest (Fig. 1). Then, we sampled the posterior (Eq. 8) using the MCMC algorithm with a simple Metropolis sampler MCMC_{METROP}IR (Martin et al. 2011) built in R environment. We generated four chains with 10^5 iterations each one, removing the first 10^4 as “burn-in”. The final convergence, checked through the potential scale factor R implemented in the CODA library (Plummer et al. 2006), is attested within 68 per cent c.l. ($R \approx 1$).

The results, median of the marginalized values of M_{200} , can be seen in Table 5. All the posteriors are unimodal, although not symmetrical (and hence the difference in the plus and minus uncertainties) and not degenerate. The higher correlations are still small – namely between the masses of A1644S and #5 (-0.25) and A1644S and #3 (-0.21).

As we can observe in Table 5 the ratio of fitted mass to mass uncertainty is smaller than the detection (e.g. Martinet et al. 2016). One possible mechanism responsible for that is the non-conformity

⁵ Corresponding to the median of each marginalized posterior.

of the model assumptions with the real clumps, for example, the absence of axisymmetry and/or a deviation from the theoretical profile.

The haloes directly related to the X-ray emission, A1644S (#2) and A1644N1 (#6), have masses of $1.90^{+0.89}_{-1.28} \times 10^{14} M_{\odot}$ and $0.90^{+0.45}_{-0.85} \times 10^{14} M_{\odot}$, respectively. Both are considerably smaller than X-ray measurements presented by Johnson et al. (2010) (A1644S: 4.6 ± 0.6 ; A1644N1: 3.8 ± 0.6). The discrepancy is noticeable but not a total surprise as the A1644 ICM is out of hydrodynamical equilibrium and this surely affects the X-ray mass estimation.

As for A1644N2 (#9) we got $M_{200} = 0.76^{+0.37}_{-0.75} \times 10^{14} M_{\odot}$. Therefore, the core of A1644 has a combined mass of $3.99^{+1.39}_{-1.59} \times 10^{14} M_{\odot}$, corresponding to the sum of the S+N1+N2 posteriors. Adding the candidate clump #5, the value increases to $5.11^{+1.32}_{-1.44} \times 10^{14} M_{\odot}$.

Substructure #3 came out of the analysis as the single most massive clump of the field, although with rather large error bars: $3.37^{+1.40}_{-2.06} \times 10^{14} M_{\odot}$. It was rather unexpected, given that its convergence peak is almost the same height as #2 (A1644S), whose nominal mass value is almost half of it. Also there are not so many cluster galaxies associated with it, assuming a I-#3 connection, nor any hints of a background structure in the photometry data. From the κ map (Fig. 6) it seems that it may have an extension or (projected) neighbours to the NW direction, which might enhance its mass somewhat.

Regarding the A1644 candidate structures, our model was not able to recover the mass of #16. The masses of #5 and #10 are $0.87^{+0.43}_{-0.82} \times 10^{14}$ and $0.56^{+0.28}_{-0.55} \times 10^{14} M_{\odot}$, respectively.

4 DYNAMICAL ANALYSIS

From the radial velocities available in the literature we explore the complex dynamical picture of A1644. We are particularly interested in verifying whether the mass substructures found through our photometric plus weak lensing analysis are actually dynamical structures bound to the main cluster.

4.1 Identification of the spectroscopic cluster members

The field of A1644 has been exhaustively observed by the Wide-field Nearby Galaxy-cluster Survey (WINGS; Fasano et al. 2006). As a result, a simple search on the NASA Extragalactic Database (NED)⁶ has revealed a total of 360 galaxies with available redshifts located inside a circular region of 33 arcmin centred on A1644S. After searching on our galaxy catalogue, we have found photometric counterparts for 341 objects whose redshift distribution can be seen in Fig. 7.

A simple approach to select the cluster spectroscopic members consists of the application of the 3- σ clipping method (Yahil & Vidal 1977). Despite its simplicity, this procedure is sufficiently accurate to remove the most obvious outliers of the sample (Wojtak et al. 2007). The resulting sample consisted of 249 galaxies with $\bar{z} = 0.0471 \pm 0.0002$ and $\sigma_z/(1 + \bar{z}) = 1017 \text{ km s}^{-17}$ (hatched region in Fig. 7). According to the Anderson-Darling test, the null

⁶ <https://ned.ipac.caltech.edu/>

⁷ The $(1 + z)^{-1}$ factors that appears multiplying velocity dispersions or differences are there to compensate for the cosmological stretching of velocities.

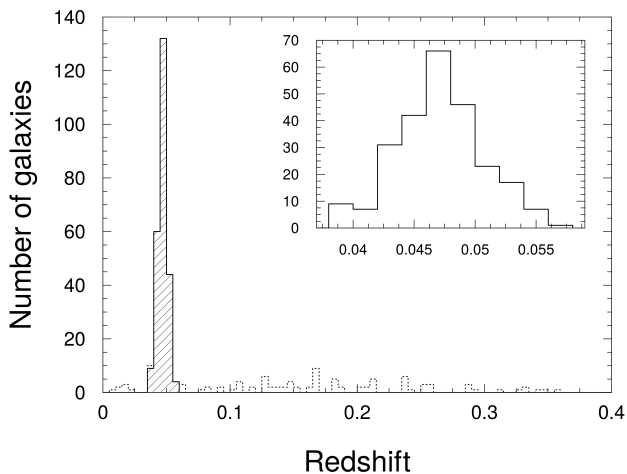


Figure 7. Redshift distribution in A1644 region. We have selected the spectroscopic cluster members after a 3σ -clipping procedure. The selected members are highlighted by hashing lines and are shown in more detail in the upper right panel. The 249 selected members have $\bar{z} = 0.0471 \pm 0.0002$ with $\sigma_v/(1+z) = 1017 \text{ km s}^{-1}$.

hypothesis of Gaussianity cannot be discarded for this sample within a confidence level of 95% (p – value = 0.21). This is in agreement with recent findings of [Lopes et al. \(2018\)](#).

Although the overall distribution of redshifts is Gaussian it does not necessarily mean that there are no substructures present. To search for those, we have applied the well-known Δ -test ([Dressler & Shectman 1988](#)), that looks for structures in both velocity space and projected position, and are described by the following equations:

$$\delta_i = \left\{ \left(\frac{N_{\text{nb}} + 1}{\sigma^2} \right) [(\bar{v}_l - \bar{v})^2 + (\sigma_l - \sigma)^2] \right\}^{1/2} \quad (9)$$

$$\Delta = \sum_{i=1}^N \delta_i. \quad (10)$$

For a cluster hosting any substructures, [Dressler & Shectman \(1988\)](#) suggest $\Delta \geq N$ as the expected statistics. However, [Hou et al. \(2012\)](#) have proposed an improved index based on the p – value < 0.01 to identify a substructure (see [Monteiro-Oliveira et al. 2017a](#), for a more complete description of this statistic).

The application of the Δ -test in our sample returned $\Delta = 339$ with a p-value of 0.007, both pointing to the presence of substructures. The spatial distribution of the spectroscopic members overlaid with the Δ -test results is shown as a “bubble plot” (Fig. 8).

The Δ -test does not identify which individual galaxies belong to a substructure. In [Monteiro-Oliveira et al. \(2017a\)](#), however, we envisaged a process to do so by searching for a threshold δ_c (equation 9). All galaxies having $\delta_i \geq \delta_c$ ⁸ were therefore considered part of some substructure and then excluded of the main sample (galaxies marked with “x” in Fig. 8).

We ended up with 210 galaxies in the main sample with similar average and dispersion than the original 249 members sample. Most

of the galaxies in substructures are spatially coincident with the mass clumps G-#10 and H-#16, previously identified as subcluster candidates. Thus, their high dynamical deviation with respect to the other members strongly suggest that both belong to a non-virialised regions being most probably infalling groups ([Einasto et al. 2018](#)).

4.2 Identifying the subclusters with MCLUST

The R-based package MCLUST ([Chris Fraley & Scrucca 2012](#)) encompasses functions designed to perform multidimensional normal mixture modelling based on the analysis of finite mixture of distributions. It works by searching for the optimized clustering of the data using models with variable shape, orientation and volume. A prior restricting the number of normal components is allowed. The output includes number and characteristics of the components plus the individual memberships. More details about the use of MCLUST to search for substructures in the observable phase space of a cluster can be found in [Einasto et al. \(2012\)](#).

At this point we already established that A1644 is composed of several substructures, probably in merger, but its 1D velocity distribution is very consistent with normalcy. It is a hint that the subclusters’ motions are taking place almost parallel to the plane of the sky (e.g. [Monteiro-Oliveira et al. 2018](#); [Wittman et al. 2018a](#)). As a consequence, one-dimensional methods, i.e. those based only on the radial velocity information, will certainly fail to assign confidently the galaxies to a host subcluster. In fact, as a confirmation, 1D-MCLUST pointed out that the single-component model is strongly favoured in relation to a bimodal distribution in the redshift space as revealed by Bayesian information criteria ([Kass & Raftery 1995](#)) as $\Delta\text{BIC} = 16$.

Given this scenario, we directed our efforts to the analysis of the spatial distribution of cluster members within the cluster core. The sample used here consists of the projected position (α and δ) of combined photometric red-sequence and spectroscopic members. Since this data is spread across all the field, we have restricted our region of interest to the inner part, selecting only the galaxies inside two circular regions, each one with a radius of 7 arcmin, centred on the BCG S and on the mid-point between A1644N1 and A1644N2. See Fig. 9 for the positions of the 163 galaxies of this sample.

The application of 2D-MCLUST showed the data are best described as a bimodal distribution. This model is strongly favoured with respect to the second-best model with three groups, as pointed out by $\Delta\text{BIC} = 12$. In both scenarios the two main groups contain most of the sample. In the case with three groups, the third one has a few galaxies on the SE direction of A1644S (or clump B-#1; Fig. 6). The outcome is a cut in the sample along the SE–NW direction, separating A1644S at one side and A1644N1/N2 at the other (orange points versus cyan and purple on Fig. 9). This division is consistent with the position of the most significant galaxy clumps according to Table 6. We also performed the exercise to include the redshift information⁹ for a tri-dimensional analysis with 3D-MCLUST. The result was a return to unimodality.

In order to understand the dynamical process that formed the complex A1644 as we see today, we are interested in estimating the relative velocities between the clumps we found both by photometry and weak lensing. In order to do that, we reran 2D-MCLUST over the northern sample it already identified and imposed a division in two groups. These results are presented in Fig. 9 (cyan versus purple

⁸ We have adopted $\delta_c = 2$ which has been shown to be a good threshold to remove the substructures.

⁹ For those galaxies for which this information is available.

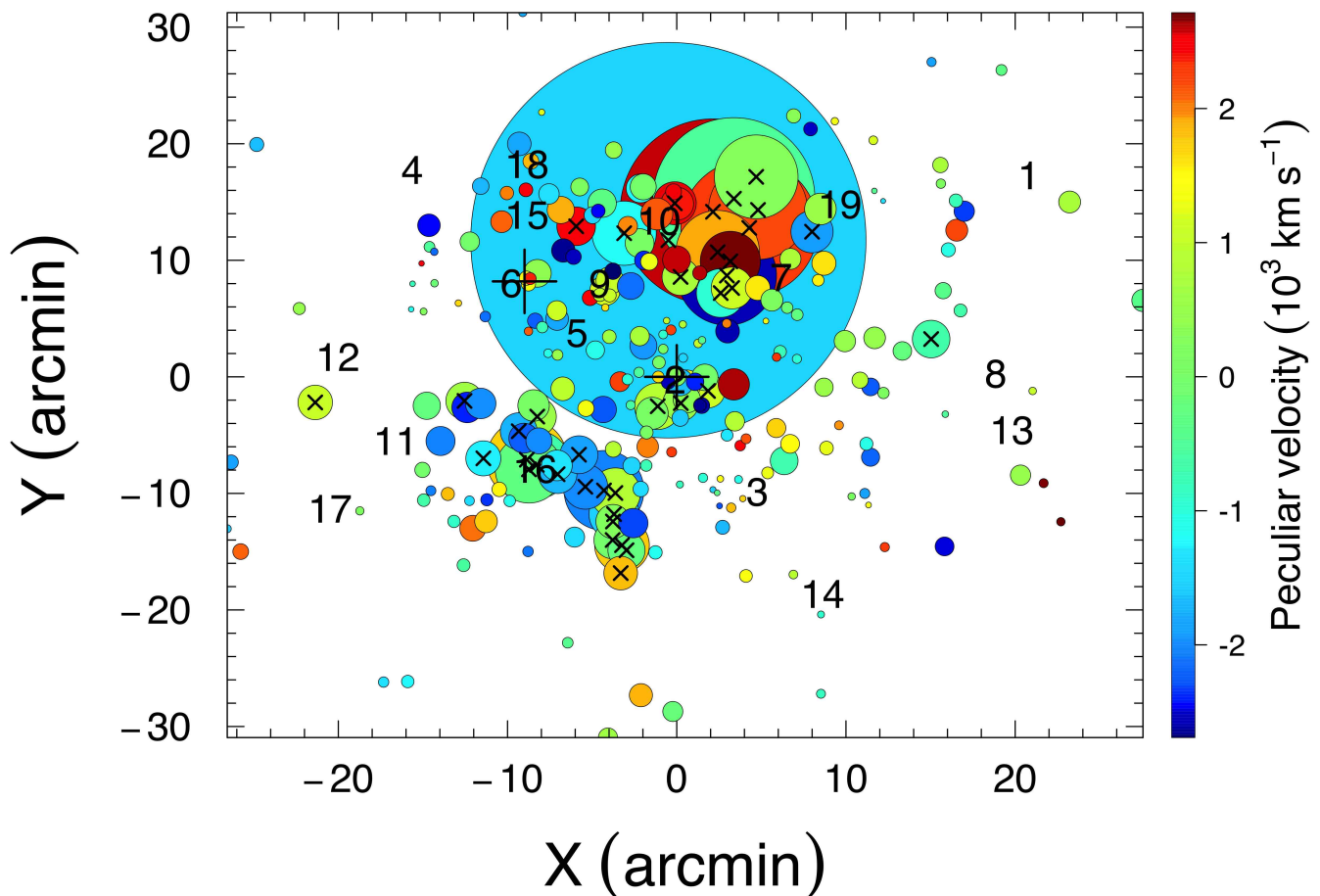


Figure 8. Bubble plot produced with Δ -test results. The filled circles indicate each galaxy position and their radius are proportional to e^{δ_i} meaning that the larger this value, the more relevant the substructure is. To make their positions clear, two “+” signals are placed at the BCGs locations. The mass clump IDs are placed at the exact place of the corresponding centre. The colour bar represents the peculiar velocities $v_i - \bar{v}$ and “x” indicates the galaxies classified as belonging to some substructure according to our $\delta_i \geq 2$ criterion. Our final sample consisted of 210 galaxies characterized by the same mean redshift and velocity dispersion of the initial sample. Note that this region is somewhat larger than those defined in Fig. 1.

points) and now we have clear samples that can be associated with each of the three main core structures (S, N1, and N2).

In Table 7, we show redshifts and velocity dispersions from the redshifts we have for each of those samples. In Table 8, we show the differences in (rest-frame) velocities. As expected we find small separations between them, in the velocity space, not inconsistent with zero given the uncertainties.

5 HYDRODYNAMICAL SIMULATIONS

In this section, we employ N -body hydrodynamical simulations to evaluate whether the newly discovered structure A1644N2 could be responsible for the collision that gave rise to the sloshing spiral. Several simulations were performed in search of a model that reproduces some of the desired morphological features of A1644. Here we present one model that successfully recovers the spiral morphology of A1644S: it is an encounter between A1644S and A1644N2

only. In the simulation presented here, A1644N1 is not included. For a more detailed analysis of the set of simulations, the reader is referred to an accompanying paper (Doubrawa et al. 2020), in which we explore the outcomes of alternative scenarios and discuss their relative advantages and disadvantages. In this section, we will describe the main features of one plausible model.

To have an acceptable scenario, some constraints must be satisfied by the simulations: the virial masses and virial radii estimated in this paper; the spiral morphology of cold gas, with an extent of approximately 200 kpc; the observed projected separation of ~ 550 kpc between the structures; and simultaneously A1644N2 must have a low fraction of gas to be nearly undetectable in X-ray observations.

Taking the new virial mass estimates, $1.9 \times 10^{14} M_{\odot}$ for A1644S and $0.76 \times 10^{14} M_{\odot}$ for A1644N2, we create two spherically symmetric galaxy clusters that are initially in hydrostatic equilibrium. The method for generating initial conditions is similar to those used in Machado & Lima Neto (2015). Each cluster is created with 2×10^6 particles, divided equally between gas and dark matter, fol-

Table 7. Statistics of galaxy groups found with 2D-MCLUST.

	A1644S	A1644N1	A1644N2
Number of galaxies	42	17	17
\bar{z}	0.0472 ± 0.0006	0.0476 ± 0.0007	0.0460 ± 0.0012
$\sigma_v/(1 + \bar{z})$ (km s ⁻¹)	1146_{-59}^{+211}	886_{-85}^{+261}	1376_{-134}^{+402}

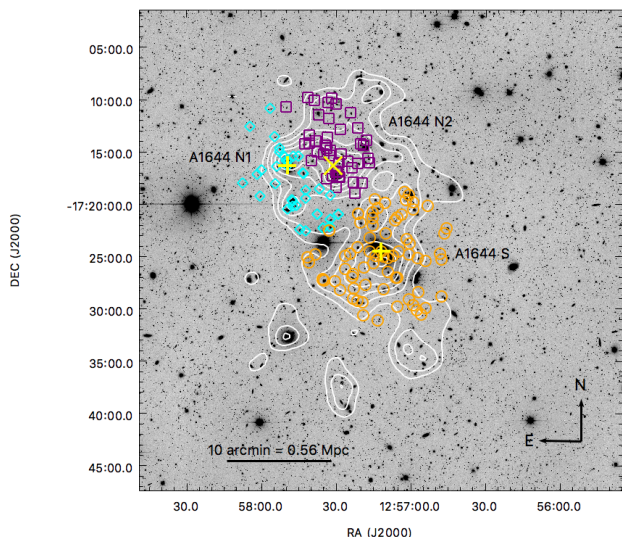

Figure 9. Galaxy classification suggested by double application of 2D-MCLUST. The picture shows the spatial distribution of the members of A1644S (orange), A1644N1 (cyan), and A1644N2 (purple) overlaid with the numerical density contours of the combined sample containing both spectroscopic and photometric members (white lines). For comparison, “+” are placed at BCGs positions and “x” marks the position of the mass clump A1644N2.

Table 8. Dynamics of the subclusters A1644S, A1644N1, and A1644N2 modelled by 2D-MCLUST. Projected distances were computed based on the respective mass peak positions. All error bars correspond to 68 per cent c.l.

Pairs	$\delta v/(1 + \bar{z})$ (km s ⁻¹)	Projected distance (kpc)
S–N1	137 ± 278	723
S–N2	334 ± 378	531
N1–N2	471 ± 397	298

lowing the procedure described in Machado & Lima Neto (2013). Simulations were carried out with GADGET-2 (Springel 2005). Initially the clusters are separated by 3 Mpc along the x -axis, with an impact parameter of $b = 800$ kpc, and initial relative velocity of -700 km s⁻¹ in the x direction (at $t = 0$). The evolution of the system is followed by 5 Gyr.

The desired configuration is achieved at $t = 4.3$ Gyr, that is, 1.6 Gyr after the pericentric passage and 0.5 Gyr after reaching the maximum separation of 770 kpc. This model presents temperature maps that are in good qualitative agreement with the expected ranges presented in Reiprich et al. (2004b) and Johnson et al. (2010). Similarly, the spiral morphology of cool gas in A1644S displays

adequate shape and extent. Fig. 10 shows the projected density, and the emission-weighted temperature map of the hydrodynamical simulation at $t = 4.3$ Gyr, highlighting the presence of A1644N2 with the symbol \times .

After the first pericentric passage, A1644N2 loses almost all of its gas, making it difficult to identify in X-ray observations. It retains about 0.1 – 1 per cent of its initial gas mass. In order to obtain a projected separation of approximately 550 kpc between clusters, at the best match of morphology, the orbital plane was inclined by $i \approx 30^\circ$ with respect to the plane of the sky. This is compatible with the low line-of-sight velocity found by the observational analysis (Table 8). We can estimate this relative velocity between A1644S and A1644N2 through the displacement between the clusters cores in the z -axis inside a short time step around $t = 4.3$ Gyr. This approach results in a line-of-sight velocity of ~ 100 km s⁻¹, in agreement with the low values expected in a merging system near their maximum separation.

Our goal was to recover the morphological features observed in A1644 through hydrodynamical simulations. To judge the adequacy of the simulation results, most comparisons were made by qualitative visual inspection of the morphology. The model presented is one of the possible combinations of the collision parameters. With this scenario, we were able to reproduce, in a best instant, several of the simulation constraints, such as morphology, temperature and extent of the sloshed gas, projected separation and low X-ray emission of A1644N2, with the virial masses and radii derived from the gravitational weak lensing analysis. Our current plausible model is thus the scenario in which A1644N2 is the disturber that induced the sloshing. Other scenarios involving A1644N1 instead of A1644N2 did not give rise to results as satisfactory as the model presented here. Alternative simulations are explored in more detail in Doubrawa et al. (2020).

6 DISCUSSION

We presented here a comprehensive analysis of the nearby merging galaxy cluster Abell 1644. With a combination of observational and computational techniques, we were able to propose a new description for the preceding collision events which led to the current state. We put forth a scenario in which the remarkable spiral-like structure seen in the X-ray emission of A1644S arose as a result of the interaction with the newly discovered subcluster A1644N2 and not due to A1644N1 as suggested by previous studies.

From large field-of-view images taken in three broad-bands, we built a careful selection of the galaxy samples. The luminosity map of the red cluster sequence galaxies (Fig. 3) brought the first hint that the cluster morphology should be somewhat more complex than previously claimed. Besides the two prominent galaxy clumps related to each BCG (A1644S and A1644N1), a third one, not reported in previous studies, was found slightly to the West of BCG N (A1644N2). Surrounding these central concentrations,

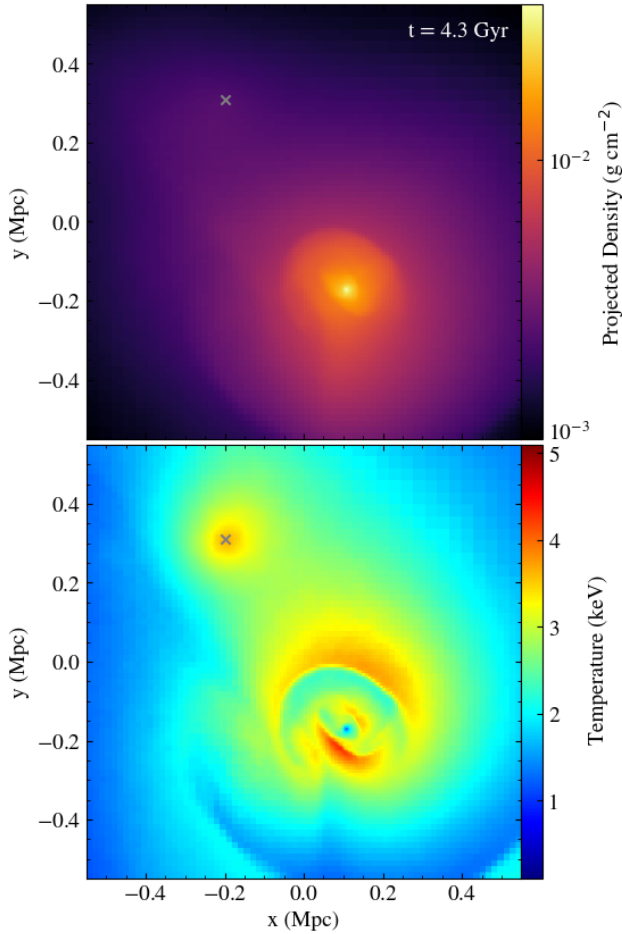


Figure 10. Top panel: Projected density map for the merger simulation between A1644S and A1644N2, at $t = 4.3$ Gyr. Bottom panel: Projected emission-weighted temperature. The symbol marks the presence of A1644N2, nearly undetectable on the density map.

two others can be found in the cluster outskirts. Further analysis based on their radial velocities, showed that they consist of infalling groups. There are also two galaxy clumps located reasonably close to significant mass concentrations, but with no spatial coincidence. With our analysis, we cannot categorically state if they are part of the cluster, though it could be possible. Conservatively, we classified both as A1644 candidates. However, for the description of the merger process among the main subclusters, the presence of such structures can be disregarded as a first approximation. These findings are illustrated in Fig. 11.

In this work, we presented the first weak-gravitational lensing recovered projected mass distribution of the extremely low- z merging cluster Abell 1644. Since this technique does not assume any prior about the dynamical state, it is a powerful tool to recover the total mass of cluster haloes. The projected mass map corroborates the scenario indicated by the projected galaxy luminosity distribution, with each of the three main galaxy concentrations related to a respective mass clump. In A1644S, the BCG matches exactly the mass clump centre whereas A1644N1 is displaced only 56 kpc in relation to that. However, projected separations up to ~ 100 kpc are not statistically significant because is also comparable with the expected effect caused by shape noise and smoothing of weak lens-

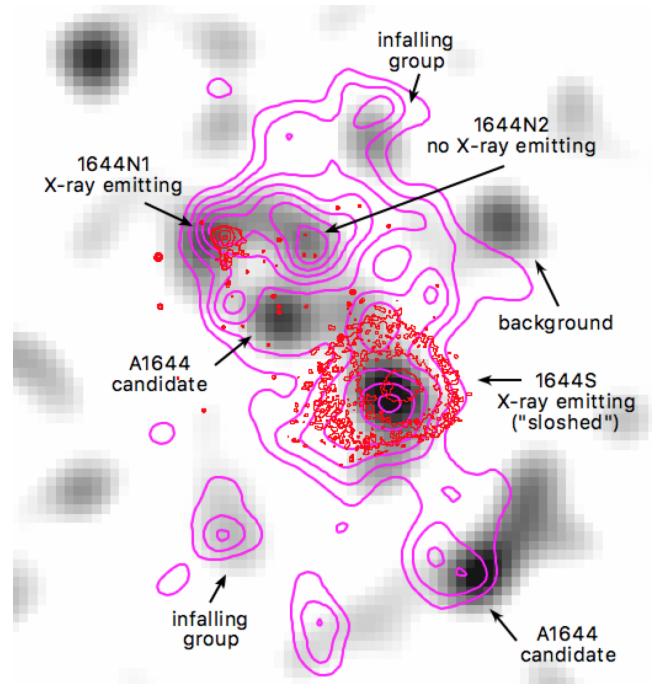


Figure 11. Proposed scenario for the merging cluster A1644. The weak lensing mass map (gray-scale) is overlaid with the r' projected galaxy luminosity distribution (magenta contours) and X-ray emission (red contours). The main subcluster, A1644S has a spiral-like pattern in its ICM distribution caused by the passage the gas-poor subcluster A1644N2, found in this work. The cluster core is also formed by the X-ray emitting subcluster A1644N1. There are also two infalling galaxy groups in the cluster vicinity. We classified as A1644 candidates two significant mass clumps surrounded by red galaxies.

ing mass maps (Dietrich et al. 2012). The three main structures are separated from each other by 723 kpc (S–N1), 531 kpc (S–N2), and 298 kpc (N1–N2). The total mass content of A1644 is evaluated in, at least, $M_{200} = 3.99^{+1.39}_{-1.59} \times 10^{14} M_{\odot}$.

From the catalogue of radial velocities available in the literature, we were able to provide some insights about the dynamics of A1644. Regarding the three main subclusters, we found that they are not so apart in relation to the line of sight, having $\delta v / (1 + \bar{z}) < 470$ km s $^{-1}$ (Table 8) and, within the uncertainties, compatible with a negligible separation (e.g. Wittman et al. 2018a).

One probe of the perturbed state of a system is how its velocity dispersion was boosted during the merger process (e.g. Pinkney et al. 1996; Takizawa et al. 2010; Monteiro-Oliveira et al. 2018). For an idealized isolated system, the pre-merger velocity dispersion σ_{pre} can be estimated from an empirical relation $M_{200} - \sigma_v$ (e.g. Biviano et al. 2006). To do this, we considered the entire sample of 4×10^5 mass values from the MCMC mass modelling (Sec. 3.3.3). We found 656^{+146}_{-109} km s $^{-1}$ for A1644S, 528^{+135}_{-107} km s $^{-1}$ for A1644N1 and 502^{+132}_{-101} km s $^{-1}$ for A1644N2. After the pericentric passage, the velocity dispersion σ_{obs} is easily obtained (see Table 7). Therefore, the boost factors $f \equiv \sigma_{\text{obs}} / \sigma_{\text{pre}}$, are $f_S = 1.8^{+0.4}_{-0.6}$, $f_{N1} = 1.7^{+0.6}_{-0.7}$ and $f_{N2} = 2.8^{+0.9}_{-1.2}$, respectively for A1644S, A1644N1 and A1644N2. The amount of events where the final velocity dispersion was not greater than unity (i.e. σ_{pre} was not enhanced by the collision) was 2 per cent, 10 per cent and 2 per cent for A1644S, A1644N1, and A1644N2, respectively. However, these results should be considered with parsimony since velocity dispersion, specially from the

Northern subclusters, was obtained with a small subset of galaxies (see Table 7).

The main finding of this work is the discovery of A1644N2. This structure presumably has a lower gas content than what would be expected for its M_{200} , since the X-ray emission map only shows gas counterparts for A1644S and A1644N1. At the position of A1644N2, the X-ray emission is not nearly as important as the others, even though its virial mass is comparable to those of A1644N1. What led to this situation?

One possible explanation is that A1644N2 suffered a recent close encounter with A1644S. If the pericentric passage was sufficiently close, A1644N2 could have been stripped of most of its gas. At the same time, its gravitational perturbation could have stirred the cool gas in the core of A1644S. This explanation has the advantage of simultaneously accounting for the two noteworthy gas features of this system: the sloshing spiral in the South and low gas content in the North. The intensity of the gas stripping in A1644N2 will depend on its precise orbit around A1644S and also on their initial gas density profiles. Similarly, the shape, size and temperature of the sloshing spiral depend on the density profiles and also on the parameters of the collision. The spiral morphology is sensitively time dependent, and so is the projected separation between the clusters. The question then would be: is there a combination of parameters capable of producing all of the desired outcomes at the same time? Our simulations provided one specific model in good qualitative agreement with the observational constraints. As is always the case in this type of modelling, one cannot ensure the uniqueness of the proposed solution. Nevertheless, the fact that a detailed model can be found indicates that a collision between A1644S and A1644N2 is indeed a feasible scenario. Other combinations of initial condition parameters are explored in greater detail in the associated paper (Doubrawa et al. 2020).

7 SUMMARY

Here, we summarize the main findings of this work.

- From our weak lensing analysis, based on deep and large field-of-view images, we have found that the merging galaxy cluster Abell 1644 ($z = 0.0471$) presents a more complex structure than described in previous works. We point here that the system is comprised not only by two but by three central subclusters, surrounded by infalling galaxy groups.

- Subclusters A1644S and A1644N1 show each one a counterpart in the hot emitting X-ray gas. Their masses are, $M_{200}^S = 1.90^{+0.89}_{-1.28} \times 10^{14} M_{\odot}$ and $M_{200}^{N1} = 0.90^{+0.45}_{-0.85} \times 10^{14} M_{\odot}$, respectively. The velocity dispersions of their galactic contents are considerably high, $\sigma_v^S = 1146^{+211}_{-59} \text{ km s}^{-1}$ and $\sigma_v^{N2} = 886^{+261}_{-85} \text{ km s}^{-1}$, respectively.

- The new structure identified in this work, A1644N2, is a gas poor subcluster, whose estimated total mass is $M_{200}^{N2} = 0.76^{+0.37}_{-0.75} \times 10^{14} M_{\odot}$. The velocity dispersion is evaluated to be $\sigma_v^{N2} = 1376^{+402}_{-134} \text{ km s}^{-1}$ based on its galaxy spectroscopic members.

- Combining the total mass distribution with the redshift catalogue of A1644 members, we identified two infalling groups at the cluster outskirts. The most massive has a mass of $M_{200} = 0.56^{+0.28}_{-0.55} \times 10^{14} M_{\odot}$.

- We performed a set of tailored hydrodynamical simulations in which an encounter between A1644S and A1644N2 was the responsible for the rise of the sloshing spiral. We offered a specific

model that accounts for several observed features, such as virial masses and radii, spiral morphology and temperature, separation and inclination. Our best model indicates that the collision is seen 1.6 Gyr after pericentric passage and that the plane of the orbit is inclined with 30° with respect to the plane of the sky. In this scenario, the two clusters have already reached the apoapsis and are currently incoming for their second approach.

Finally, we note that the full details of the set of hydrodynamical simulations are described in the companion paper (Doubrawa et al. 2020), where we explore alternative scenarios and also investigate what role A1644N1 might have played in the dynamics of this complex system.

ACKNOWLEDGEMENTS

We thank the anonymous referee for his/her suggestions that contributed to the improvement of the paper. This work has made use of the computing facilities of the Laboratory of Astroinformatics (IAG/USP, NAT/Unicsul), whose purchase was made possible by the Brazilian agency FAPESP (grant 2009/54006-4) and the INCT-A. Simulations were carried out in part at the Centro de Computação Científica e Tecnológica (UTFPR). This study was financed in part by the *Coordenação de Aperfeiçoamento de Pessoal de Nível Superior - Brasil* (CAPES) - Finance Code 001. RMO acknowledges support from CAPES. REGM acknowledges support from the Brazilian agency *Conselho Nacional de Desenvolvimento Científico e Tecnológico* (CNPq) through grants 303426/2018-7 and 406908/2018-4. GBLN thanks financial support from CNPq and FAPESP (grant 2018/17543-0). ESC acknowledges support from the CNPq through grant 308539/2018-4. This work is based in part on data products produced at Terapix available at the Canadian Astronomy Data Centre as part of the Canada-France-Hawaii Telescope Legacy Survey, a collaborative project of NRC and CNRS. We made use of the NASA/IPAC Extragalactic Database, which is operated by the Jet Propulsion Laboratory, California Institute of Technology, under contract with NASA. This research draws upon DECam data as distributed by the Science Data Archive at NOAO. NOAO is operated by the Association of Universities for Research in Astronomy (AURA) under a cooperative agreement with the National Science Foundation.

REFERENCES

- Adelman-McCarthy J. K., 2011, *VizieR Online Data Catalog*, 2306
Andrade-Santos F., Lima Neto G. B., Laganá T. F., 2012, *ApJ*, 746, 139
Ascasibar Y., Markevitch M., 2006, *ApJ*, 650, 102
Beers T. C., Geller M. J., Huchra J. P., 1982, *ApJ*, 257, 23
Biviano A., Murante G., Borgani S., Diaferio A., Dolag K., Girardi M., 2006, *A&A*, 456, 23
Blanton E. L., Randall S. W., Clarke T. E., Sarazin C. L., McNamara B. R., Douglass E. M., McDonald M., 2011, *ApJ*, 737, 99
Bridle S. L., Hobson M. P., Lasenby A. N., Saunders R., 1998, *MNRAS*, 299, 895
Chris Fraley Adrian E. Raftery T. B. M., Scrucca L., 2012, mclust Version 4 for R: Normal Mixture Modeling for Model-Based Clustering, Classification and Density Estimation. <http://CRAN.R-project.org/package=mclust>
Clowe D., Gonzalez A., Markevitch M., 2004, *ApJ*, 604, 596
Clowe D., Bradač M., Gonzalez A. H., Markevitch M., Randall S. W., Jones C., Zaritsky D., 2006, *ApJ*, 648, L109
Cypriano E. S., Sodré Laerte J., Campusano L. E., Kneib J.-P., Giovanelli R., Haynes M. P., Dale D. A., Hardy E., 2001, *AJ*, 121, 10

- Cypriano E. S., Sodré Jr. L., Kneib J.-P., Campusano L. E., 2004, *ApJ*, **613**, 95
- Dawson W. A., 2013, *ApJ*, **772**, 131
- Dietrich J. P., Böhnert A., Lombardi M., Hilbert S., Hartlap J., 2012, *MNRAS*, **419**, 3547
- Doubrawa L., Machado R. E. G., Laganá T. F., Monteiro-Oliveira R., Lima Neto G. B., Cypriano E. S., 2020, *MNRAS*, submitted
- Dressler A., Shectman S. A., 1988, *AJ*, **95**, 985
- Duffy A. R., Schaye J., Kay S. T., Dalla Vecchia C., 2008, *MNRAS*, **390**, L64
- Einasto M., et al., 2012, *A&A*, **540**, A123
- Einasto M., et al., 2018, *A&A*, **610**, A82
- Ettori S., Fabian A. C., White D. A., 1997, *MNRAS*, **289**, 787
- Fasano G., et al., 2006, *A&A*, **445**, 805
- Girardi M., Escalera E., Fadda D., Giuricin G., Mardirossian F., Mezzetti M., 1997, *ApJ*, **482**, 41
- Girardi M., Giuricin G., Mardirossian F., Mezzetti M., Boschin W., 1998, *ApJ*, **505**, 74
- Harvey D., et al., 2014, *MNRAS*, **441**, 404
- Harvey D., Massey R., Kitching T., Taylor A., Tittley E., 2015, *Science*, **347**, 1462
- Hetterscheidt M., Erben T., Schneider P., Maoli R., van Waerbeke L., Mellier Y., 2005, *A&A*, **442**, 43
- Hou A., et al., 2012, *MNRAS*, **421**, 3594
- Johnson R. E., Markevitch M., Wegner G. A., Jones C., Forman W. R., 2010, *ApJ*, **710**, 1776
- Jones C., Forman W., 1999, *ApJ*, **511**, 65
- Kass R. E., Raftery A. E., 1995, *Journal of the American Statistical Association*, **90**, 773
- Lacey C., Cole S., 1993, *MNRAS*, **262**, 627
- Laganá T. F., Andrade-Santos F., Lima Neto G. B., 2010, *A&A*, **511**, A15
- Liu J., Haiman Z., 2016, *Phys. Rev. D*, **94**, 043533
- Lopes P. A. A., Trevisan M., Laganá T. F., Durret F., Ribeiro A. L. B., Rembold S. B., 2018, *MNRAS*, **478**, 5473
- Machado R. E. G., Lima Neto G. B., 2013, *MNRAS*, **430**, 3249
- Machado R. E. G., Lima Neto G. B., 2015, *MNRAS*, **447**, 2915
- Machado R. E. G., Monteiro-Oliveira R., Lima Neto G. B., Cypriano E. S., 2015, *MNRAS*, **451**, 3309
- Markevitch M., Vikhlinin A., 2007, *Phys. Rep.*, **443**, 1
- Markevitch M., Vikhlinin A., Mazzotta P., 2001, *ApJ*, **562**, L153
- Markevitch M., Gonzalez A. H., Clowe D., Vikhlinin A., Forman W., Jones C., Murray S., Tucker W., 2004, *ApJ*, **606**, 819
- Marshall P. J., Hobson M. P., Gull S. F., Bridle S. L., 2002, *MNRAS*, **335**, 1037
- Martin A. D., Quinn K. M., Park J. H., 2011, *Journal of Statistical Software*, **42**, 22
- Martinet N., et al., 2016, *A&A*, **590**, A69
- Medezinski E., Broadhurst T., Umetsu K., Oguri M., Rephaeli Y., Benítez N., 2010, *MNRAS*, **405**, 257
- Medezinski E., et al., 2018, *PASJ*, **70**, 30
- Mellier Y., 1999, *ARA&A*, **37**, 127
- Meylan G., Jetzer P., North P., Schneider P., Kochanek C. S., Wambsgans J., eds, 2006, *Gravitational Lensing: Strong, Weak and Micro* ([arXiv:astro-ph/0407232](https://arxiv.org/abs/astro-ph/0407232))
- Monteiro-Oliveira R., Cypriano E. S., Machado R. E. G., Lima Neto G. B., Ribeiro A. L. B., Sodré L., Dupke R., 2017a, *MNRAS*, **466**, 2614
- Monteiro-Oliveira R., Lima Neto G. B., Cypriano E. S., Machado R. E. G., Capelato H. V., Laganá T. F., Durret F., Bagchi J., 2017b, *MNRAS*, **468**, 4566
- Monteiro-Oliveira R., Cypriano E. S., Vitorelli A. Z., Ribeiro A. L. B., Sodré L., Dupke R., Mendes de Oliveira C., 2018, *MNRAS*, **481**, 1097
- Navarro J. F., Frenk C. S., White S. D. M., 1996, *ApJ*, **462**, 563
- Navarro J. F., Frenk C. S., White S. D. M., 1997, *ApJ*, **490**, 493
- Nychka D., Furrer R., Sain S., 2014, *Fields: Tools for spatial data*. <http://CRAN.R-project.org/package=fields>
- O'Mill A. L., Proust D., Capelato H. V., Castejon M., Cypriano E. S., Neto G. B. L., Laerte S., 2015, *MNRAS*, **453**, 868
- Pandge M. B., Monteiro-Oliveira R., Bagchi J., Simionescu A., Limousin M., Raychaudhury S., 2019, *MNRAS*, **482**, 5093
- Pinkney J., Roettiger K., Burns J. O., Bird C. M., 1996, *ApJS*, **104**, 1
- Plummer M., Best N., Cowles K., Vines K., 2006, *R News*, **6**, 7
- R Core Team 2014, *R: A Language and Environment for Statistical Computing*. R Foundation for Statistical Computing, Vienna, Austria, <http://www.R-project.org/>
- Reiprich T. H., Sarazin C. L., Kempner J. C., Tittley E., 2004a, *ApJ*, **608**, 179
- Reiprich T. H., Sarazin C. L., Kempner J. C., Tittley E., 2004b, *ApJ*, **608**, 179
- Sanders J. S., et al., 2020, *A&A*, **633**, A42
- Sarazin C. L., 2004, *Journal of Korean Astronomical Society*, **37**, 433
- Schirmer M., 2004, PhD thesis, Rheinischen Friedrich-Wilhelms-Universität Bonn
- Schneider P., 1996, *MNRAS*, **283**, 837
- Schneider P., 2005, *ArXiv Astrophysics e-prints*,
- Seitz S., Schneider P., Bartelmann M., 1998, *A&A*, **337**, 325
- Springel V., 2005, *MNRAS*, **364**, 1105
- Springel V., et al., 2005, *Nature*, **435**, 629
- Takizawa M., Nagino R., Matsushita K., 2010, *PASJ*, **62**, 951
- Tustin A. W., Geller M. J., Kenyon S. J., Diaferio A., 2001, *AJ*, **122**, 1289
- Valdes F., Gruendl R., DES Project 2014, in Manset N., Forshay P., eds, *Astronomical Society of the Pacific Conference Series Vol. 485, Astronomical Data Analysis Software and Systems XXIII*. p. 379
- Walker S. A., ZuHone J., Fabian A., Sanders J., 2018, *Nature Astronomy*, **2**, 292
- Wei C., Li G., Kang X., Liu X., Fan Z., Yuan S., Pan C., 2018, *MNRAS*, **478**, 2987
- Wittman D., Cornell B. H., Nguyen J., 2018a, *ApJ*, **862**, 160
- Wittman D., Golovich N., Dawson W. A., 2018b, *ApJ*, **869**, 104
- Wojtak R., Lokas E. L., Mamon G. A., Gottlöber S., Prada F., Moles M., 2007, *A&A*, **466**, 437
- Wright E. L., 2006, *PASP*, **118**, 1711
- Yahil A., Vidal N. V., 1977, *ApJ*, **214**, 347
- Yang X., Kratochvil J. M., Huffenberger K., Haiman Z., May M., 2013, *Phys. Rev. D*, **87**, 023511

This paper has been typeset from a $\text{\TeX}/\text{\LaTeX}$ file prepared by the author.